Biomedical Optics EXPRESS

Repeatability of in vivo 3D lamina cribrosa microarchitecture using adaptive optics spectral domain optical coherence tomography

Zach Nadler,[1] Bo Wang,[1,2] Gadi Wollstein,[1,*] Jessica E. Nevins,[1] Hiroshi Ishikawa,[1,2] Richard Bilonick,[1,2] Larry Kagemann,[1,2] Ian A. Sigal,[1,2] R. Daniel Ferguson,[3] Ankit Patel,[3] Daniel X. Hammer,[4] Joel S. Schuman[1,2]

[1]UPMC Eye Center, Eye and Ear Institute, Ophthalmology and Visual Science Research Center, University of Pittsburgh School of Medicine, Pittsburgh, Pennsylvania, USA

[2]Department of Bioengineering, Swanson School of Engineering, University of Pittsburgh, Pittsburgh, Pennsylvania, USA

[3]Physical Science Inc., Andover, Massachusetts, USA

[4]Center for Devices and Radiological Health, Food and Drug Administration, Silver Spring, Maryland, USA

[*]wollsteing@upmc.edu

Abstract: We demonstrate the repeatability of lamina cribrosa (LC) microarchitecture for in vivo 3D optical coherence tomography (OCT) scans of healthy, glaucoma suspects, and glaucomatous eyes. Eyes underwent two scans using a prototype adaptive optics spectral domain OCT (AO-SDOCT) device from which LC microarchitecture was semi-automatically segmented. LC segmentations were used to quantify pore and beam structure through several global microarchitecture parameters. Repeatability of LC microarchitecture was assessed qualitatively and quantitatively by calculating parameter imprecision. For all but one parameters (pore volume) measurement imprecision was <4.7% of the mean value, indicating good measurement reproducibility. Imprecision ranged between 27.3% and 54.5% of the population standard deviation for each parameter, while there was not a significant effect on imprecision due to disease status, indicating utility in testing for LC structural trends.

OCIS codes: (100.2000) Digital image processing; (170.4470) Ophthalmology; (110.4500) Optical coherence tomography; (170.1610) Clinical applications; (330.4460) Ophthalmic optics and devices.

References and links

1. H. A. Quigley, "Glaucoma: macrocosm to microcosm the Friedenwald lecture," Invest. Ophthalmol. Vis. Sci. **46**(8), 2663–2670 (2005).
2. H. A. Quigley and A. T. Broman, "The number of people with glaucoma worldwide in 2010 and 2020," Br. J. Ophthalmol. **90**(3), 262–267 (2006).
3. K. A. Townsend, G. Wollstein, and J. S. Schuman, "Imaging of the retinal nerve fibre layer for glaucoma," Br. J. Ophthalmol. **93**(2), 139–143 (2009).
4. G. Wollstein, H. Ishikawa, J. Wang, S. A. Beaton, and J. S. Schuman, "Comparison of three optical coherence tomography scanning areas for detection of glaucomatous damage," Am. J. Ophthalmol. **139**(1), 39–43 (2005).
5. C. K. S. Leung, S. Lam, R. N. Weinreb, S. Liu, C. Ye, L. Liu, J. He, G. W. K. Lai, T. Li, and D. S. Lam, "Retinal nerve fiber layer imaging with spectral-domain optical coherence tomography: analysis of the retinal nerve fiber layer map for glaucoma detection," Ophthalmology **117**(9), 1684–1691 (2010).
6. O. Tan, G. Li, A. T.-H. Lu, R. Varma, and D. Huang; Advanced Imaging for Glaucoma Study Group, "Mapping of macular substructures with optical coherence tomography for glaucoma diagnosis," Ophthalmology **115**(6), 949–956 (2008).
7. O. Tan, V. Chopra, A. T.-H. Lu, J. S. Schuman, H. Ishikawa, G. Wollstein, R. Varma, and D. Huang, "Detection of macular ganglion cell loss in glaucoma by Fourier-domain optical coherence tomography," Ophthalmology **116**(12), 2305 (2009).
8. F. A. Medeiros, L. M. Zangwill, C. Bowd, R. M. Vessani, R. Susanna, Jr., and R. N. Weinreb, "Evaluation of retinal nerve fiber layer, optic nerve head, and macular thickness measurements for glaucoma detection using

#202060 - $15.00 USD Received 26 Nov 2013; revised 4 Feb 2014; accepted 21 Feb 2014; published 10 Mar 2014

optical coherence tomography," Am. J. Ophthalmol. **139**(1), 44–55 (2005).
9. E. J. Lee, T.-W. Kim, R. N. Weinreb, K. H. Park, S. H. Kim, and D. M. Kim, "Visualization of the lamina cribrosa using enhanced depth imaging spectral-domain optical coherence tomography," Am. J. Ophthalmology **152**(1), 87–95 (2011).
10. H.-Y. L. Park, S. H. Jeon, and C. K. Park, "Enhanced depth imaging detects lamina cribrosa thickness differences in normal tension glaucoma and primary open-angle glaucoma," Ophthalmology **119**(1), 10–20 (2012).
11. C. Alexandrescu, A. M. Dascalu, A. Panca, A. Sescioreanu, C. Mitulescu, R. Ciuluvica, L. Voinea, and C. Celea, "Confocal scanning laser ophthalmoscopy in glaucoma diagnosis and management," J. Med. Life **3**(3), 229–234 (2010).
12. D. Ng, L. M. Zangwill, L. Racette, C. Bowd, J. P. Pascual, R. R. A. Bourne, C. Boden, R. N. Weinreb, and P. A. Sample, "Agreement and repeatability for standard automated perimetry and confocal scanning laser ophthalmoscopy in the diagnostic innovations in glaucoma study," Am. J. Ophthalmol. **142**(3), 381–386 (2006).
13. N. G. Strouthidis, S. Demirel, R. Asaoka, C. Cossio-Zuniga, and D. F. Garway-Heath, "The Heidelberg retina tomograph Glaucoma Probability Score: reproducibility and measurement of progression," Ophthalmology **117**(4), 724–729 (2010).
14. A. S. Vilupuru, N. V. Rangaswamy, L. J. Frishman, E. L. Smith 3rd, R. S. Harwerth, and A. Roorda, "Adaptive optics scanning laser ophthalmoscopy for in vivo imaging of lamina cribrosa," J. Opt. Soc. Am. A **24**(5), 1417–1425 (2007).
15. T. Akagi, M. Hangai, K. Takayama, A. Nonaka, S. Ooto, and N. Yoshimura, "In vivo imaging of lamina cribrosa pores by adaptive optics scanning laser ophthalmoscopy," Invest. Ophthalmol. Vis. Sci. **53**(7), 4111–4119 (2012).
16. K. M. Ivers, C. Li, N. Patel, N. Sredar, X. Luo, H. Queener, R. S. Harwerth, and J. Porter, "Reproducibility of measuring lamina cribrosa pore geometry in human and nonhuman primates with in vivo adaptive optics imaging," Invest. Ophthalmol. Vis. Sci. **52**(8), 5473–5480 (2011).
17. S. Kiumehr, S. C. Park, D. Syril, C. C. Teng, C. Tello, J. M. Liebmann, and R. Ritch, "In vivo evaluation of focal lamina cribrosa defects in glaucoma," Arch. Ophthalmol. **130**(5), 552–559 (2012).
18. A. J. Tatham, A. Miki, R. N. Weinreb, L. M. Zangwill, and F. A. Medeiros, "Defects of the lamina cribrosa in eyes with localized retinal nerve fiber layer loss," Ophthalmology **121**, 110–118 (2014).
19. B. Wang, J. E. Nevins, Z. Nadler, G. Wollstein, H. Ishikawa, R. A. Bilonick, L. Kagemann, I. A. Sigal, I. Grulkowski, J. J. Liu, M. Kraus, C. D. Lu, J. Hornegger, J. G. Fujimoto, and J. S. Schuman, "In vivo lamina cribrosa micro-architecture in healthy and glaucomatous eyes as assessed by optical coherence tomography," Invest. Ophthalmol. Vis. Sci. **54**(13), 8270–8274 (2013).
20. L. Fontana, A. Bhandari, F. W. Fitzke, and R. A. Hitchings, "In vivo morphometry of the lamina cribrosa and its relation to visual field loss in glaucoma," Curr. Eye Res. **17**(4), 363–369 (1998).
21. G. Tezel, K. Trinkaus, and M. B. Wax, "Alterations in the morphology of lamina cribrosa pores in glaucomatous eyes," Br. J. Ophthalmol. **88**(2), 251–256 (2004).
22. N. Sredar, K. M. Ivers, H. M. Queener, G. Zouridakis, and J. Porter, "3D modeling to characterize lamina cribrosa surface and pore geometries using in vivo images from normal and glaucomatous eyes," Biomed. Opt. Express **4**(7), 1153–1165 (2013).
23. C. Torti, B. Povazay, B. Hofer, A. Unterhuber, J. Carroll, P. K. Ahnelt, and W. Drexler, "Adaptive optics optical coherence tomography at 120,000 depth scans/s for non-invasive cellular phenotyping of the living human retina," Opt. Express **17**(22), 19382–19400 (2009).
24. R. J. Zawadzki, S. S. Choi, A. R. Fuller, J. W. Evans, B. Hamann, and J. S. Werner, "Cellular resolution volumetric in vivo retinal imaging with adaptive optics–optical coherence tomography," Opt. Express **17**(5), 4084–4094 (2009).
25. Z. Nadler, B. Wang, G. Wollstein, J. E. Nevins, H. Ishikawa, L. Kagemann, I. A. Sigal, R. D. Ferguson, D. X. Hammer, I. Grulkowski, J. J. Liu, M. F. Kraus, C. D. Lu, J. Hornegger, J. G. Fujimoto, and J. S. Schuman, "Automated lamina cribrosa microstructural segmentation in optical coherence tomography scans of healthy and glaucomatous eyes," Biomed. Opt. Express **4**(11), 2596–2608 (2013).
26. D. X. Hammer, R. D. Ferguson, M. Mujat, A. Patel, E. Plumb, N. Iftimia, T. Y. P. Chui, J. D. Akula, and A. B. Fulton, "Multimodal adaptive optics retinal imager: design and performance," J. Opt. Soc. Am. A **29**(12), 2598–2607 (2012).
27. J. Schindelin, I. Arganda-Carreras, E. Frise, V. Kaynig, M. Longair, T. Pietzsch, S. Preibisch, C. Rueden, S. Saalfeld, B. Schmid, J. Y. Tinevez, D. J. White, V. Hartenstein, K. Eliceiri, P. Tomancak, and A. Cardona, "Fiji: an open-source platform for biological-image analysis," Nat. Methods **9**(7), 676–682 (2012).
28. T. Y. Zhang and C. Y. Suen, "A fast parallel algorithm for thinning digital patterns," Commun. ACM **27**(3), 236–239 (1984).
29. M. Doube, M. M. Kłosowski, I. Arganda-Carreras, F. P. Cordelières, R. P. Dougherty, J. S. Jackson, B. Schmid, J. R. Hutchinson, and S. J. Shefelbine, "BoneJ: Free and extensible bone image analysis in ImageJ," Bone **47**(6), 1076–1079 (2010).
30. R. Rezakhaniha, A. Agianniotis, J. T. C. Schrauwen, A. Griffa, D. Sage, C. V. C. Bouten, F. N. van de Vosse, M. Unser, and N. Stergiopulos, "Experimental investigation of collagen waviness and orientation in the arterial adventitia using confocal laser scanning microscopy," Biomech. Model. Mechanobiol. **11**(3-4), 461–473 (2012).
31. J. L. Jaech, *Statistical Analysis of Measurement Errors (Exxon Monographs Series)*, 1 ed. (Wiley 1985).

#202060 - $15.00 USD Received 26 Nov 2013; revised 4 Feb 2014; accepted 21 Feb 2014; published 10 Mar 2014

32. J. M. Bland and D. G. Altman, "Statistical methods for assessing agreement between two methods of clinical measurement," Lancet **327**(8476), 307–310 (1986).
33. J. W. Bartlett and C. Frost, "Reliability, repeatability and reproducibility: analysis of measurement errors in continuous variables," Ultrasound Obstet. Gynecol. **31**(4), 466–475 (2008).
34. M. D. Roberts, V. Grau, J. Grimm, J. Reynaud, A. J. Bellezza, C. F. Burgoyne, and J. C. Downs, "Remodeling of the connective tissue microarchitecture of the lamina cribrosa in early experimental glaucoma," Invest. Ophthalmol. Vis. Sci. **50**(2), 681–690 (2008).
35. H. A. Quigley and E. M. Addicks, "Regional differences in the structure of the lamina cribrosa and their relation to glaucomatous optic nerve damage," Arch. Ophthalmol. **99**(1), 137–143 (1981).
36. M. Winkler, B. Jester, C. Nien-Shy, S. Massei, D. S. Minckler, J. V. Jester, and D. J. Brown, "High resolution three-dimensional reconstruction of the collagenous matrix of the human optic nerve head," Brain Res. Bull. **81**(2-3), 339–348 (2010).
37. R. Grytz, G. Meschke, and J. B. Jonas, "The collagen fibril architecture in the lamina cribrosa and peripapillary sclera predicted by a computational remodeling approach," Biomech. Model. Mechanobiol. **10**(3), 371–382 (2011).
38. L. Dandona, H. A. Quigley, A. E. Brown, and C. Enger, "Quantitative regional structure of the normal human lamina cribrosa. A racial comparison," Arch. Ophthalmol. **108**(3), 393–398 (1990).
39. I. A. Sigal, J. G. Flanagan, I. Tertinegg, and C. R. Ethier, "3D morphometry of the human optic nerve head," Exp. Eye Res. **90**(1), 70–80 (2010).

1. Introduction

The lamina cribrosa (LC) is a collagen based meshwork structure within the optic nerve head (ONH) and is the supportive tissue surrounding retinal nerve fibers as they exit the eye [1]. It is thought to play an important role in the pathogenesis of glaucoma, which is an optic neuropathy marked by irreversible loss of the retinal ganglion cells. This loss is associated with functional visual defect and is the second leading cause of blindness worldwide [2]. Given the progressive and irreversible nature of the disease, considerable effort has been invested in developing methods of early glaucoma detection. Optical coherence tomography (OCT) and confocal scanning laser ophthalmoscopy (CSLO) are two clinical ocular imaging technologies that enable in vivo quantitative assessment of ocular structures. OCT studies of glaucoma commonly focus on retinal nerve fiber layer thickness [3–5], as well as the thickness of other retinal layers [4,6–8], and more recently the anterior lamina surface in the ONH and LC thickness [9,10], while CSLO primarily targets ONH topography [11–13] and more recently LC pore and beam structure using adaptive optics (AO) [14–16].

Because the LC is located deep within the ONH, OCT imaging is typically of limited use because of the reduced signal at greater depths. The development of enhanced depth imaging (EDI), a technique where the complex conjugate image is used to counterbalance signal losses from depth attenuation, has allowed current commercial technology to probe to the level of the LC [10]. In addition, longer wavelength light sources enable better light penetration into the tissue. Consequently, in vivo investigation of LC performed so far have probed local irregularities in the anterior surface of the lamina [17], assessed of full thickness defects [18], and most recently differences in quantitative pore and beam structure was considered in healthy and glaucomatous eyes using swept source OCT (SS-OCT) [19]. Other in vivo studies have investigated laminar pore shape and size using fundus photography [20,21] and CSLO images, but these lack high axial and transverse resolution as well as tissue penetration, which is a limitation when evaluating a 3D structure, such as the LC. A potential solution is the combination of the two technologies, which provide detailed lateral resolution (AO-CSLO) with detailed cross-sectional information (OCT) [22].

OCT imaging has recently been augmented with adaptive optics, a technique for correcting for optical aberrations in the eye. When combined with AO, spectral-domain (SD) OCT can achieve a four-fold improvement in lateral resolution compared with conventional OCT, and can generate high-resolution 3D volumes of the area of interest. Using this technology individual LC pores have been imaged in 3D [23,24]. In a previous study we proposed a novel, semi-automated segmentation of the LC micro-architecture that has been developed for 3D OCT images [25]. That method was used in the SS-OCT study of pore and beam structure, in which repeatability was assessed on a subset of the study population

#202060 - $15.00 USD Received 26 Nov 2013; revised 4 Feb 2014; accepted 21 Feb 2014; published 10 Mar 2014

revealing high precision for all parameters besides overall pore count. However, performance discrepancies noted between AO-SDOCT and SS-OCT in the development of the automated segmentation method and the physical differences in underlying imaging technology suggests the translation of high repeatability in one device to the other is nontrivial. The purpose of this study is to validate this method by evaluating the repeatability of 3D AO-SDOCT LC segmentation analysis.

2. Methods

Healthy, glaucoma suspects, and glaucoma subjects were enrolled at the University of Pittsburgh Medical Center (UPMC) Eye Center. The study was approved by the University of Pittsburgh's Institutional Review Board. All subjects provided informed consent prior to enrollment and the study was conducted in adherent to the tenets of the Declaration of Helsinki.

All participants underwent comprehensive ophthalmic examination, visual field testing (Humphrey Field Analyzer, Zeiss, Dublin, CA) and scanning with the AO-SDOCT system. Diagnosis of glaucoma was determined by the presence of typical glaucomatous findings in the fundus examination (optic disc rim notching, cup asymmetry, large cupping (vertical cup to disc ratio >0.7), retinal nerve fiber layer defect or intraocular pressure >21 mmHg) and visual field. Glaucoma suspect consisted of individuals with ocular hypertension, optic nerve head changes as defined above, or the contralateral eye of a glaucomatous eye, all in the presence of full visual field. One eye was randomly selected for the study if both eyes qualified. Each subjects' pupils were dilated with proparacaine and tropicamide and the eyes were scanned twice using a prototype multimodal AO retinal imaging system (Physical Sciences Inc., Andover, MA) [26]. The system combines CSLO and SDOCT imaging channels with AO correction to achieve transverse and axial resolutions of ~5μm and ~4.5μm, respectively in the eye; nearly four times better than standard transverse resolution in commercial SDOCT. The light source for the AO-SDOCT was a 1050nm central wavelength SLED, permitting greater tissue penetration than the standard 850nm sources present in most commercial SDOCT systems.

Scanning was performed in 6°x6° square centered on the ONH. The scan density was 1024 A-lines per B-Scan, each with a depth of 512 pixels, and 200 B-scans per volume at a scanning rate of 28kHz. Scan times were approximately 7 seconds. Scans were acquired in the same imaging session within minutes of one another.

After acquisition, AO-SDOCT data volumes underwent a series of standard image processing techniques carried out in the FIJI software suite [27]: AO-SDOCT B-scans are co-registered to the center of CSLO frames, which were inspected for movement artifacts during scanning and warped B-Scans were removed. Frame-to-frame cross-correlation extracted shift information between adjacent CSLO frames (Fig. 1), which was then used to build a 3D data cube by interpolating the gaps between AO-SDOCT B-scans. 3D Gaussian blur with a 2 pixel $\sigma_{x,y}$ and 3 pixel σ_z was applied to remove high frequency noise.

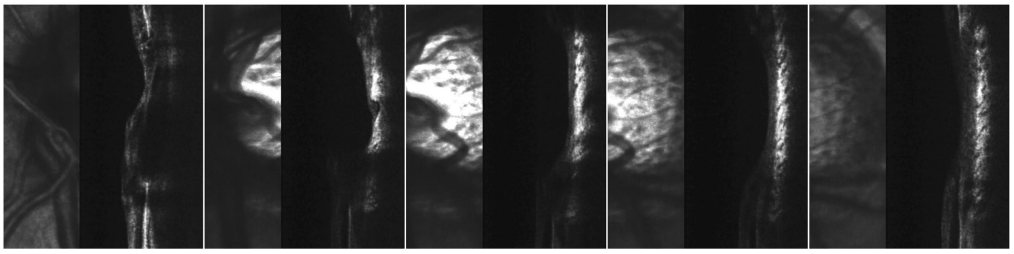

Fig. 1. 6° scan of the lamina cribrosa taken as the confocal scanning laser ophthalmoscopy (CSLO) frame pans horizontally across the volume. AO-SDOCT (right of each pane) shows the tissue cross-section corresponding to the center of the CSLO frame, which is then used to register and reconstruct the volume.

#202060 - $15.00 USD Received 26 Nov 2013; revised 4 Feb 2014; accepted 21 Feb 2014; published 10 Mar 2014

The processed 3D stack was resliced into coronal sections (C-mode). A customized segmentation algorithm utilizing an auto local thresholding method provided segmentation of LC pore structure [25]. The outer boundary of the hyper-reflective porous region defined as the LC was delineated manually in 3D where high contrast of internal micro-architecture was visible using C-mode slices. Subjective analysis of segmentation was performed on C-mode slices determined to be in similar locations for repeated scans. Beams were skeletonized using a thinning binarized algorithm provided by ImageJ that was described in detail elsewhere [28].

Several microstructural parameters were automatically generated by the automated segmentation including: mean pore area, pore diameter, beam thickness, pore volume, the ratio of beam thickness to pore diameter, and connective tissue volume fraction (CTVF). Mean pore area was calculated as the average of all pores in the LC and excluded pores below a threshold of $80\mu m^2$ to reduce the influence of local segmentation noise on measurement. Pore diameter and beam thickness were computed using the BoneJ plugin for FIJI [29]. The thickness at a given location is defined as the radius of the largest sphere containing that point within the segmented volume. All thickness values were then averaged to provide a global mean. Thickness measurements were performed in true 3D; all other measurements were performed on serial 2D slices through the entire 3D stack. The CTVF is the ratio of beam volume to the total LC volume. Using the OrientationJ plugin in FIJI, beam orientation was computed based on pixel intensity gradients, which was then masked to the LC segmentation [30]. Orientation parameters were computed using an eight pixel kernel size, chosen as approximately ¾ of standard beam diameters, and applied using a cubic spline algorithm for calculating intensity gradient, selected within the OrientationJ plugin, which evaluates local orientation for every pixel in the image. These values come from a structure tensor, which incorporates a Gaussian weighting function that was previously described in detail [30].

The en face mean intensity projections were used to identify the geometric centers of the LC. When the entire LC could not be visualized this point was estimated. The center point was then used to divide the LC into quadrants for sectoral analysis using lines which ran at 45° and 135° with respect to the horizontal meridian, creating inferior, superior, nasal and temporal quadrants. Distributions for parameters such as the histogram of beam orientations were then subjectively evaluated on a global and sectoral basis and the distribution of cross-sectional pore area and pore thickness was considered for the full image stack.

Using the scan-derived microarchitecture parameters we computed the imprecision standard deviation using the paired measurements from repeat scans. The imprecision is defined as the standard deviation of the paired differences for all subjects divided by $\sqrt{2}$ [31]. Repeatability is often expressed as a repeatability coefficient following the approach of Bland and Altman [32,33]. While we also considered Bland-Altman plots as they relate to the distribution of pore diameters for an entire 3D volume, the best estimate of measurement error is by means of imprecision standard deviation, which summarize the typical size of random measurement error. Confidence intervals were determined for our imprecision estimates, which were then compared with the overall average.

3. Results

Nine healthy, 5 glaucoma suspects and 12 glaucomatous eyes (7 left eyes 19 right) of 26 subjects were included in this study. The participants included 13 men and 13 women with a mean age of 53.3 ± 20.6 years. For healthy and glaucoma suspects the average visual field mean deviations (MD) were −0.33 ± 1.92 dB and −0.79 ± 1.09 dB respectively while for glaucoma subjects the average MD was −7.82 ± 7.48 dB.

The 3D LC structure was extracted through pore and beam segmentation of C-mode slices and quantified using parameters such as beam thickness (Fig. 2).

#202060 - $15.00 USD Received 26 Nov 2013; revised 4 Feb 2014; accepted 21 Feb 2014; published 10 Mar 2014

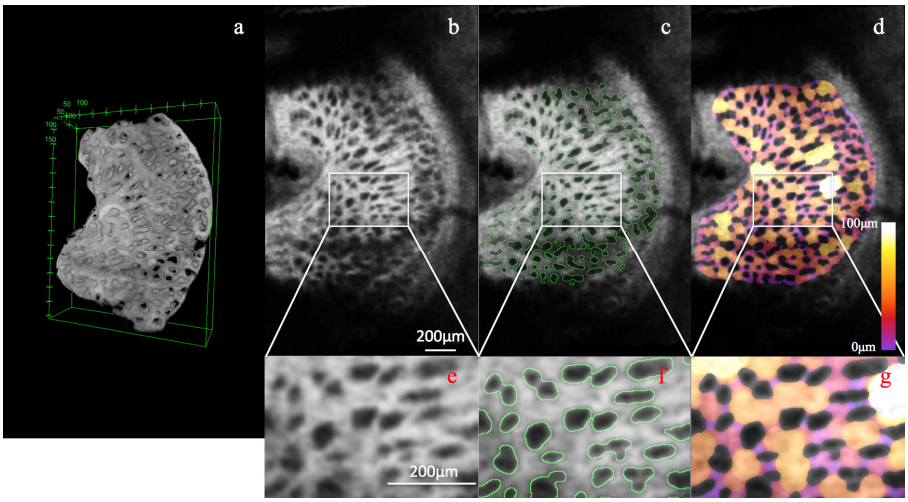

Fig. 2. 3D LC (a) and C-scan (b,e) visualization (a) is segmented in C-mode slices (c,f) permitting the quantification of structural parameters such as beam thickness where thicker beams are shown in yellow and thinner beams are purple (d,g).

Subjective evaluation of repeated scans shows structural agreement when considering pores and beams in C-mode slices at similar depth (Fig. 3). Structural agreement of pores and beams was typically better in local regions of the slice than across the full plane. Discrepancies in skeletonization were either due to beams visualized in only one scan or as an artifact of the skeletonization process, where progressive thinning within the algorithm lead to parallel beam skeletons which appeared slightly shifted from one another seen as parallel green and red lines in Fig. 3.

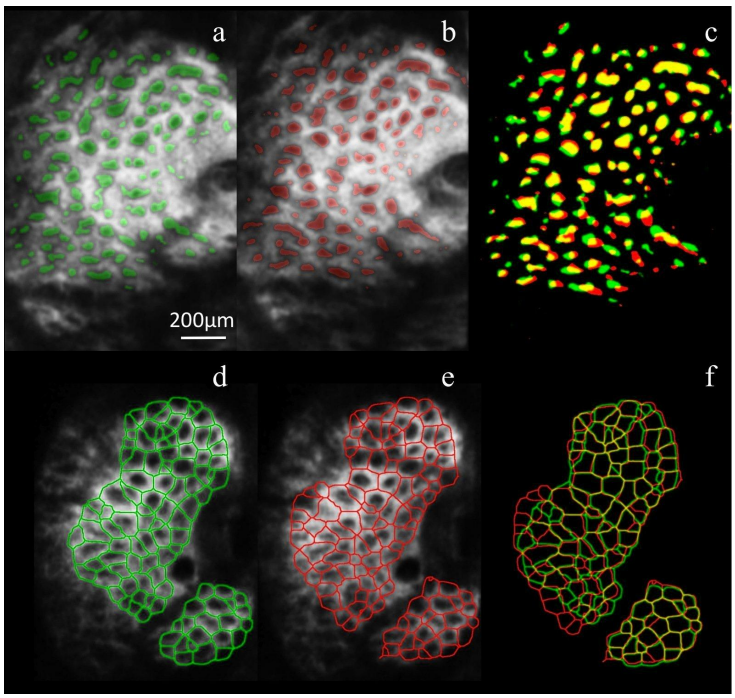

Fig. 3. Repeated C-mode slices of the same eye with pore segmentation (a, b) and skeleton presentation of the beams (d, e). Segmentation is overlaid on C-mode from similar location and compared with yellow color representing full agreement (c, f).

#202060 - $15.00 USD Received 26 Nov 2013; revised 4 Feb 2014; accepted 21 Feb 2014; published 10 Mar 2014

Distribution of parameters such as the cross-sectional areas of pores for all C-mode slices in the LC, and the orientation angle of beams showed subjective similarity in distribution shape (Fig. 4, 5). In both cases vertical shifts correspond to differences in the extent of analyzable LC, while horizontal shifts in the orientation angle histogram correspond to relative rotation between scans. Bland-Altman plots for different percentiles of the pore diameter showed consistent spread, demonstrating only minor dependence of measurement error on the size of the structure under consideration (Fig. 6).

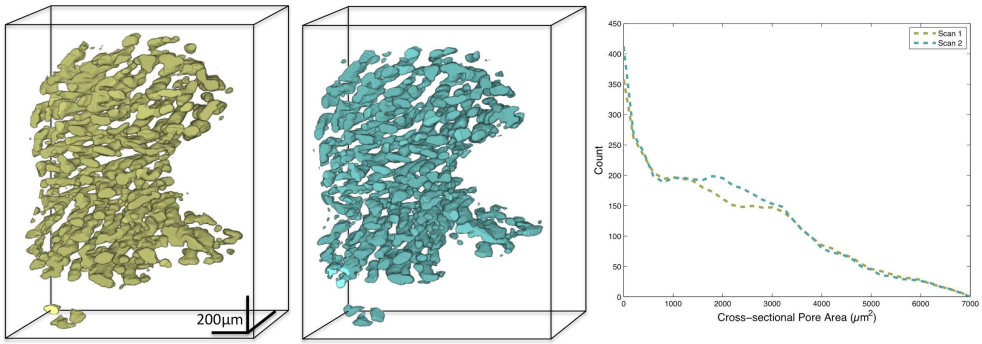

Fig. 4. Pore volumes for repeat scans visualized in 3D (left) and histogram of cross-sectional pore area (right) sampled in C-mode slices shows qualitative agreement between scans. Differences in visualizable lamina manifest as differences in pore count for excluded pores.

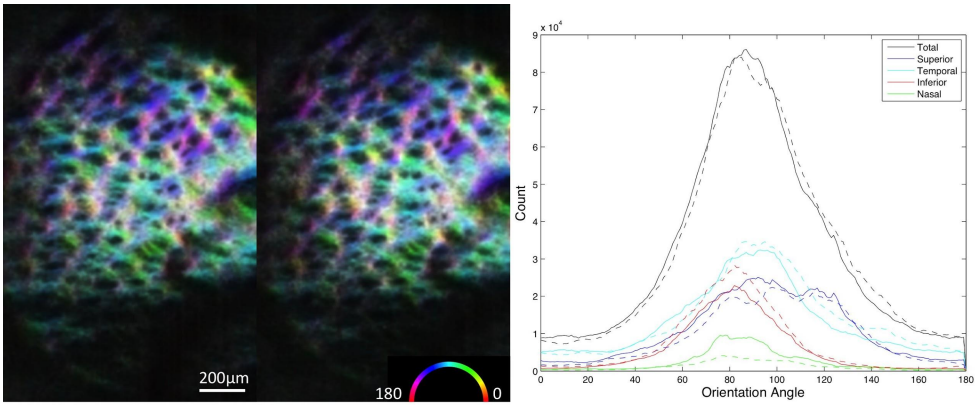

Fig. 5. C-mode slices taken from repeated scans of a glaucomatous eye are colored by beam orientation (left) which translates to a similar distribution shape for beam orientation angle between scans (right). Orientation analysis includes all C-mode slices in the LC.

Table 1 shows a summary of the average value for each parameter along with the imprecision for each subgroup of the population. Imprecision values are also expressed as percentages of the population mean. For the full population the imprecision as a percentage of the mean value for each parameter were ≤4.7% for all parameters (except for laminar volume), reflecting an overall high repeatability of the measurements. In addition, for the entire cohort, imprecision ranged between 27.3% and 54.5% of the population standard deviation for each parameter.

#202060 - $15.00 USD Received 26 Nov 2013; revised 4 Feb 2014; accepted 21 Feb 2014; published 10 Mar 2014

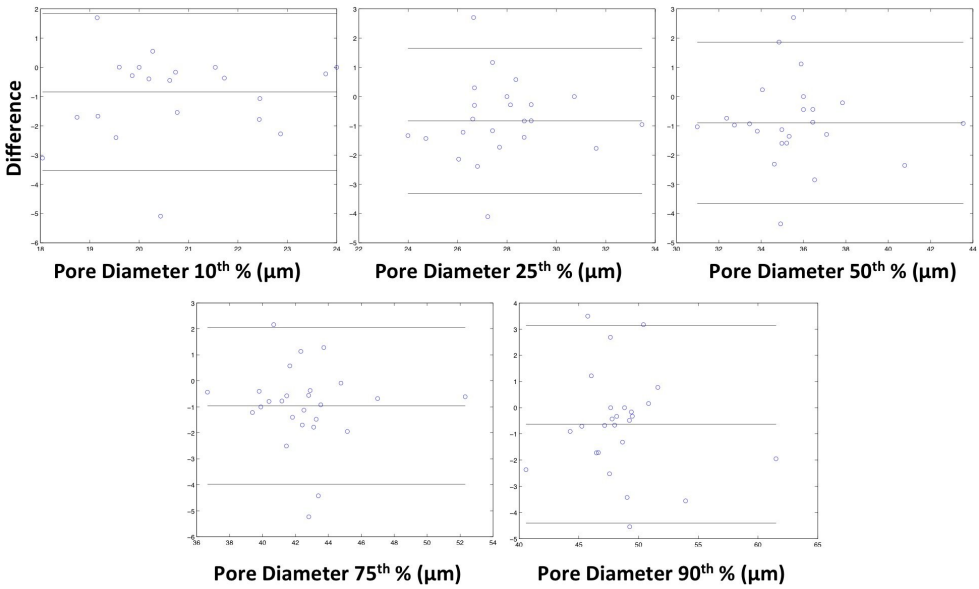

Fig. 6. Bland-Altman plots of pore diameter separated by distribution percentile. Lines show the 95% confidence intervals for paired differences. Measurement spread is fairly consistent through all pore sizes.

Table 1. Mean parameter values for segmentations of LC and their imprecision

	Mean±SD			Imprecision SD (CI)			% Imprecision SD		
	H	*GS*	*Gl*	*H*	*GS*	*Gl*	*H*	*GS*	*Gl*
Mean Pore Area (μm^2)	2412 ±509	2122 ±301	2190 ±305	169 (81, 229)	172 (69, 454)	134 (68, 156)	7.0	8.1	6.1
Pore Diameter (µm)	36.2 ±3.5	34.7 ±1.2	34.3 ±1.5	0.7 (0.3, 0.9)	1.2 (0.5, 3.2)	1.2 (0.6, 1.4)	1.8	3.5	3.4
Pore Diameter SD (µm)	11.1 ±1.7	10.3 ±0.4	10.7 ±0.7	0.3 (0.2, 0.4)	0.4 (0.1, 1.0)	0.3 (0.2, 0.4)	2.9	3.5	3.4
Beam Thickness (µm)	46.8 ±6.6	48.8 ±3.2	47.5 ±3.5	3.0 (1.5, 4.2)	3.0 (1.2, 7.9)	1.3 (0.7, 1.6)	6.6	6.3	2.8
Beam-Pore Ratio	1.29 ±0.12	1.41 ±0.09	1.39 ±0.11	0.08 (0.04, 0.11)	0.11 (0.04, 0.29)	0.07 (0.03, 0.09)	6.1	7.8	5.3
CTVF (%)	68.0 ±2.8	71.1 ±2.6	70.9 ±2.8	1.4 (0.7, 1.9)	1.0 (0.4, 2.7)	1.6 (0.8, 1.9)	2.0	1.5	2.3
Lamina Volume (mm^3)	0.0201 ±0.0123	0.0269 ±0.0228	0.0186 ±0.0097	0.0046 (0.0022, 0.0062)	0.0083 (0.0033, 0.0219)	0.0025 (0.0013, 0.0029)	22.8	30.9	13.6

H – Healthy; GS – Glaucoma suspect; Gl – Glaucoma; SD – Standard deviation; CTVF – Connective Tissue Volume Fraction; CI – 95% Confidence Interval

4. Discussion

This study was designed to test the repeatability of 3D LC microarchitecture measurements derived from AO-SDOCT scans in healthy and glaucomatous eyes. Because the LC is considered a primary site for glaucomatous damage, a robust automated method for 3D LC segmentation and quantification is desirable. Previous work using the SS-OCT with the automated segmentation algorithm showed high precision for the structural quantification method for select global parameters, but differences in the underlying technology, and observed variation in segmentation performance necessitate a thorough study to validate the repeatability of the method using AO-SDOCT [19,25]. AO-SDOCT with a 1050nm light source was used in this study because it provided high transverse and axial resolution imaging with good tissue penetration for optimal visualization and analysis of in vivo LC

#202060 - $15.00 USD Received 26 Nov 2013; revised 4 Feb 2014; accepted 21 Feb 2014; published 10 Mar 2014

microarchitecture. The sampled population included the typical mixture of subjects seen in academic glaucoma service to closely reflect the common clinical scenario. This study demonstrated that our automated 3D LC segmentation has high repeatability with imprecisions of ≤4.7% of mean parameter values in all parameters except lamina volume, and that disease status did not show an overall effect on imprecision estimates. Imprecision consistently showed values of a fraction of the parameter standard deviation for the population. This indicates that quantitative LC microarchitecture can be used for assessing longitudinal changes associated with disease.

In the qualitative evaluation of microarchitecture, similar pore and beam structure was observed on repeated scans when visualized as C-mode slices and in 3D. The overlap of pore and beam segmentations in C-mode tended to show better agreement in local regions of the image, and some discrepancy further away. This could be attributable to variable 3D rotation of the structure relative to the scanning window (tilt) or an error in B-scan alignment during 3D LC volume reconstruction. Beam skeletonization was prone to similar disagreement where skeletonized beams appeared slightly shifted between scans. This is likely a result of the same rotational shifts, or an artifact of the skeletonization process. Skeletonization also showed dissent between scans in regions where low contrast connective tissue created ambiguity about differentiating adjacent pores.

In both C-mode and 3D there were apparent differences in the peripheral extent of segmentation reflecting the variability of manually selecting the external boundary between scans. This was seen when comparing pore size distributions for repeated scans, where pores of a certain size may have been absent from a scan if they were not included in the analyzed portion of the LC. Bland-Altman plots of the pore diameter for different percentiles of the size distribution show a fairly consistent measurement error at all scales, which is a small fraction of the overall mean pore width. This indicates that structure excluded from one scan did not preferentially affect features of a certain size and the overall shape of the distribution was relatively robust. Beam orientation histograms showed similar vertical shift in overall count and some horizontal shift corresponding to relative rotation. Previous ex vivo work has considered beam orientation and the distribution of beam orientation, and pore sizes on a sectoral basis [34–36]. Detailed examination of beam orientations and deformations in response to induced stress may provide a means of examining biomechanical stress within the LC [37]. This requires robust measurement of orientation angle and the consistency demonstrated in fiber distribution suggests a possible tool for future studies investigating stress in vivo.

Inter-scan variation contributing to imprecision variably affects different parameters, but the results suggest all parameters except for pore volume demonstrate robust measurement. Lamina volume changes with observable segment of LC and the relatively high imprecision emphasizes the difficulty in manually choosing the external LC boundary. Conversely, all other microarchitecture parameters are less influenced by changes in the amount of segmented tissue, exhibiting much lower imprecision. CTVF displayed the lowest imprecision with respect to the mean, which is likely because it is the least sensitive to noise in the automated segmentation. One of the difficulties of automated segmentation is the tendency to merge distinct pores separated by small beams with low contrast (Fig. 2) [25]. The relatively low imprecision indicates that merging occurs consistently between scans or that low contrast regions in the AO-SDOCT images make up a relatively small fraction of measurement area. Pore area measurements of 2256μm^2 were comparable to previous reported values [16,38]. The exclusion of small pores increased this average from 1668μm^2, which is more characteristic of reported pore sizes for the central temporal portions of the LC, and a best estimate should fall between these values. Visualization of the peripheral LC microarchitecture is often obscured, therefore it is reasonable that AO-SDOCT measurements reflect values predominantly for the central region. The utility of these measurements in identifying trends associated with worsening disease will be considered in future work.

#202060 - $15.00 USD Received 26 Nov 2013; revised 4 Feb 2014; accepted 21 Feb 2014; published 10 Mar 2014

Consideration of independent subpopulations of this study revealed slight variation when it came to pore diameter and beam thickness. Even within these measurements confidence intervals showed that there was no significant difference. All other parameters yielded similar values for imprecision, indicating that the measurements are capable of assessing structural trends across a population. Differences may be attributable to the limited size of each subgroup. The use of imprecision standard deviation was selected for this study because it provided a good summary of the typical measurement error associated with this method of structural quantification. While the imprecision estimate provides typical measurement error, the upper bound of the 95% confidence interval gives a more absolute means of comparing structures, either between subjects or time-points. For instance in the case of glaucomatous beam width: if successive visits of a single eye reveal a beam thickness difference of greater that 1.6μm, the structure has likely undergone changes.

There are limitations to in vivo measurements of LC microarchitecture. For one, the observed region of the LC is only a small fraction of the total LC and because the structure is located deep within the ONH, viewing is obstructed by neural tissue, vasculature, peripapillary sclera, and other reflective structures anterior in the ONH [39]. Therefore within an individual we fail to capture the entirety of LC microarchitecture, and across individuals we are visualizing different portions of the LC. However, this inevitable limitation is related to the fundamental properties of OCT and should be considered when 3D properties of the LC are investigated. For the purpose of the current study this limitation has a minor effect since we are merely investigating the repeatability of measurements within an individual. Also, AO, which is useful for optimizing resolution in a system, may worsen the image when passing over a structure with variable reflectivity at different focal planes. AO corrects to the highly reflective beacon beam, which in general is the LC when appropriately focused, but during a scan the beam passes from one side of the LC across to the other and thus may apply inappropriate correction at the LC margins where the focal shift gradient is largest. In addition, AO reduces the depth of focus in the system, which may serve to improve parameter estimates in the en face plane but could further detriment the ability to resolve posterior structure, in spite of the 1050nm light source.

In conclusion, 3D LC microarchitecture parameters obtained by AO-SDOCT are repeatable, enabling their use as robust parameters for quantifying 3D LC structure in further studies in glaucomatous and healthy eyes.

Acknowledgments

The authors acknowledge this work would not have been possible without funding and support from: NIH R01-EY013178, R44-EY018986, P30-EY008098; Eye and Ear Foundation (Pittsburgh, PA); Research to Prevent Blindness (New York, NY).

Conflict of Interest: R.D. Ferguson is an employee of Physical Sciences Inc. D.X. Hammer is a former employee and a current consultant to Physical Sciences Inc. and Dr. Schuman receives royalties for an optical coherence tomography patent owned and licensed by the Massachusetts Institute of Technology and Massachusetts Eye & Ear Infirmary to Zeiss (Dublin, CA).

Disclaimer: The mention of commercial products, their sources, or their use in connection with material reported herein is not to be construed as either an actual or implied endorsement of such products by the US Department of Health and Human Services.

#202060 - $15.00 USD Received 26 Nov 2013; revised 4 Feb 2014; accepted 21 Feb 2014; published 10 Mar 2014